



Mapping clay minerals in an open-pit mine using hyperspectral and LiDAR data

Richard J. Murphy*, Zachary Taylor, Sven Schneider and Juan Nieto

Australian Centre for Field Robotics, University of Sydney, NSW, Australia, 2006

*Corresponding author, e-mail address: richard.murphy@sydney.edu.au

Abstract

The ability to map clay minerals on vertical geological surfaces is important from perspectives of stratigraphic mapping and safety. Clay minerals were mapped from hyperspectral imagery using Automated Feature Extraction and their areal coverage estimated on a complex geological surface (a mine pit) by automatically registering hyperspectral to LiDAR data. The area of the mine pit covered by each identified mineral was under- or over-estimated by as much as a factor of 2 when derived from the hyperspectral imagery alone compared to imagery co-registered to LiDAR data. Hyperspectral imagery enabled the identification of clay layers on a mine face as a means of separating geological units of similar visual or spectral characteristics.

Keywords: Mine face, hyperspectral imagery, LiDAR, clay minerals, absorption feature.

Introduction

There have been many studies which have used hyperspectral imagery acquired from aircraft to map clay minerals [e.g. Crósta et al., 1998; Lagacherie et al., 2008]. Clays and other phyllosilicates exhibit diagnostic absorptions between 2000 - 2500 nm caused by metal ions bound to hydroxyl. The location of these features depends upon several factors predominantly the type of metal cation involved. Features near 2200 nm are associated with Al-rich minerals and absorptions between 2290-2310 nm, 2330-2340 nm and 2350-2370 nm related to minerals rich in Fe^{3+} , Mg or Fe^{2+} , respectively. These diagnostic absorptions cause different minerals to have different spectral curve shapes between 2000-2500 nm. Although the majority of hyperspectral imagery has to date been collected from airborne platforms, there has been an increasing trend for imagery to be collected from field based platforms to map minerals as they are distributed on vertical outcrops of geology [Murphy et al., 2012; Kurz et al., 2013; Murphy and Monteiro, 2013]. Various sensor and environmental effects make the calibration and analysis of these data more challenging [reviewed by Kurz et al., 2013], so methods used to extract information from hyperspectral data must be resistant to these effects.

The ability to recognise clays in outcrops of vertical geology is important for geological mapping and safety perspectives. Thin bands of shale are sometimes used as marker horizons to distinguish different geological units which exhibit similar visual or spectral characteristics. Shales with large amounts of clay also represent lines of stratigraphical weakness along which landslides can occur [Hutchinson, 1961; Cornforth, 2005; Hancox, 2008]. Smectite group clays in particular can undergo large changes in volume through swelling which can cause localised instability and ground heave [Gill et al., 1996; Goetz et al., 2001]. Many techniques have been developed to classify minerals on the basis of their entire spectral curve in the ShortWave InfraRed (SWIR) where diagnostic absorption features of many minerals are located. However, several parameters of absorption features such as their wavelength position and depth can yield important information about aspects of the physical-chemical composition of minerals [Martínez-Alonso et al., 2002; Bishop et al., 2008]. To determine the identity and abundance of minerals on the mine wall we automatically identify the strongest absorption feature in each spectrum using Automated Feature Extraction (AFE). AFE has been used in previous studies to detect and parameterise absorption features without the need for a spectral library [Kruse, 1988; Murphy, 1995; Murphy et al., 2014]. AFE enables clay and other minerals to be identified and quantified without *a priori* knowledge of the surface or study area in question. AFE parameterises the deepest absorption feature in each spectrum in terms of its wavelength position (as an indicator of mineral type), depth (as an indicator of mineral abundance) and width (providing, in combination with wave length position, information on mineral type).

Translating two dimensional images representing mineral absorption within a three dimensional space into meaningful georeferenced maps is challenging, particularly for areas such as mine pits which have a complex surface geometries [Hartley and Zisserman, 2004]. The usefulness of information on the distribution of minerals in such environments is severely constrained if they are not integrated with appropriate geometric information. For example, pixels in a hyperspectral image acquired from the bottom of a mine pit may comprise a continuum of spatial resolutions i.e. they describe different areas on the surface depending on how close the surface is to the sensor. In the case of an open-pit mine, distances from sensor to target can vary from a few metres to hundreds of metres. Calculating the true surface areas occupied by the different mineral categories mapped from the hyperspectral imagery can only be done by combining (i.e. co-registering) the data with some form of geometric information, such as that obtained by LiDAR. Previous studies have registered these different types of data manually using reference targets within imagery [Zhang and Pless, 2004; Buckley et al., 2013]. Whilst this has been shown to be effective, it is not a feasible approach where data are to be acquired on a routine, operational basis to provide information on mineralogy, for example, as part of large-scale operational mining operations. Therefore to generate 2.5D maps (i.e. 3D maps of mineralogy at the surface of the mine pit) we apply an automatic registration method to register maps of mineralogy derived from hyperspectral imagery to LiDAR data [Taylor et al., 2013]. From these registered data we quantify the area of the mine pit which is occupied by each category of mineral.

Rocks of different chemical or mineral composition may have reflectance spectra which are very similar. This can be caused by the rocks being comprised of minerals which do not exhibit discrete spectral signatures - for example silica. However, in the context of vertical mine faces, variability in incident light also occurs causing spatial variability in reflectance

which may exceed that caused by the intrinsic compositional makeup of the rocks. In such cases it is not possible to uniquely separate and map units of rock on mine faces. Field geologists, using traditional mapping techniques, often use clay layers as marker horizons to separate rock units of similar visual or spectral appearance. The potential therefore exists for this to also be done automatically using hyperspectral imagery.

The objectives of this paper are therefore twofold. First, detect and quantify clay minerals over a large section of the mine pit and estimate their areal coverage (Objective 1). To do this, mineral maps derived by AFE are automatically registered with LiDAR data of the mine pit. Second, demonstrate the application of hyperspectral imagery to identify clay layers with the objective of delimiting geological units on an individual mine face which otherwise could not be distinguished using their spectral qualities alone (Objective 2). To address these problems we use hyperspectral and LiDAR data acquired from an open-pit iron-ore mine in the Pilbara, Western Australia.

Materials and methods

Study area and rock samples

The study area is located in an open-pit iron-ore mining operation in the Pilbara, Western Australia (Fig. 1a). Hyperspectral images were acquired from a single mine pit within the operation. For Objective 2, 5 replicate rock samples were acquired from different geological units and from the clay layers which delineate them (Fig. 1b). Quantitative X-Ray Diffraction (XRD) analyses of the samples were done to provide information about the weight percent of the dominant minerals within each sample. Samples were powdered in a ring mill and micronized for five minutes. XRD patterns were obtained using a Bruker-AXS D8 Advance Diffractometer with cobalt radiation. Crystalline phases were identified by using a search/match algorithm (DIFFRAC.EVA 2.1; Bruker-AXS, Germany). Relevant crystal structures extracted for refinement were obtained from the Inorganic Crystal Structure Database (ICSD 2012/1). The crystalline phases were determined on an absolute scale using Rietveld quantitative phase refinement, using the Bruker-AXS TOPAS v4.2 software package. Quantification of clay minerals from powdered samples can be prone to errors caused by a lack of sensitivity. Interpretation of XRD analyses used for ground truth should therefore be done with caution.

Hyperspectral imagery

Imagery was acquired from vertical section of the entire pit (Objective 1; Fig. 1a) and from a small section of an individual mine face (Objective 2; Fig. 1b). Hyperspectral imagery (970 – 2500 nm) was acquired using an AISA HAWK hyperspectral imager (Specim, Finland). The sensor records 320 spatial pixels (across track). The along track dimension is built up by rotating the sensor on a motorized scanning platform. The number of spectral bands recorded was 256, each having a nominal width (full-width-half-maximum) of ~6.32 nm. High temperatures (> 55° C) and wind-blown goethitic dust in the mine pit required that the sensor was enclosed in an insulated box and kept cool by passing cooled, desiccated air over it. Calibration panels with different reflectances (80 % Teflon, 15 %, 30 %, 60 % and 99 % Spectralon) were placed in the field of view of the sensor. Data were acquired under clear-sky conditions with the sun directly illuminating the mine wall.

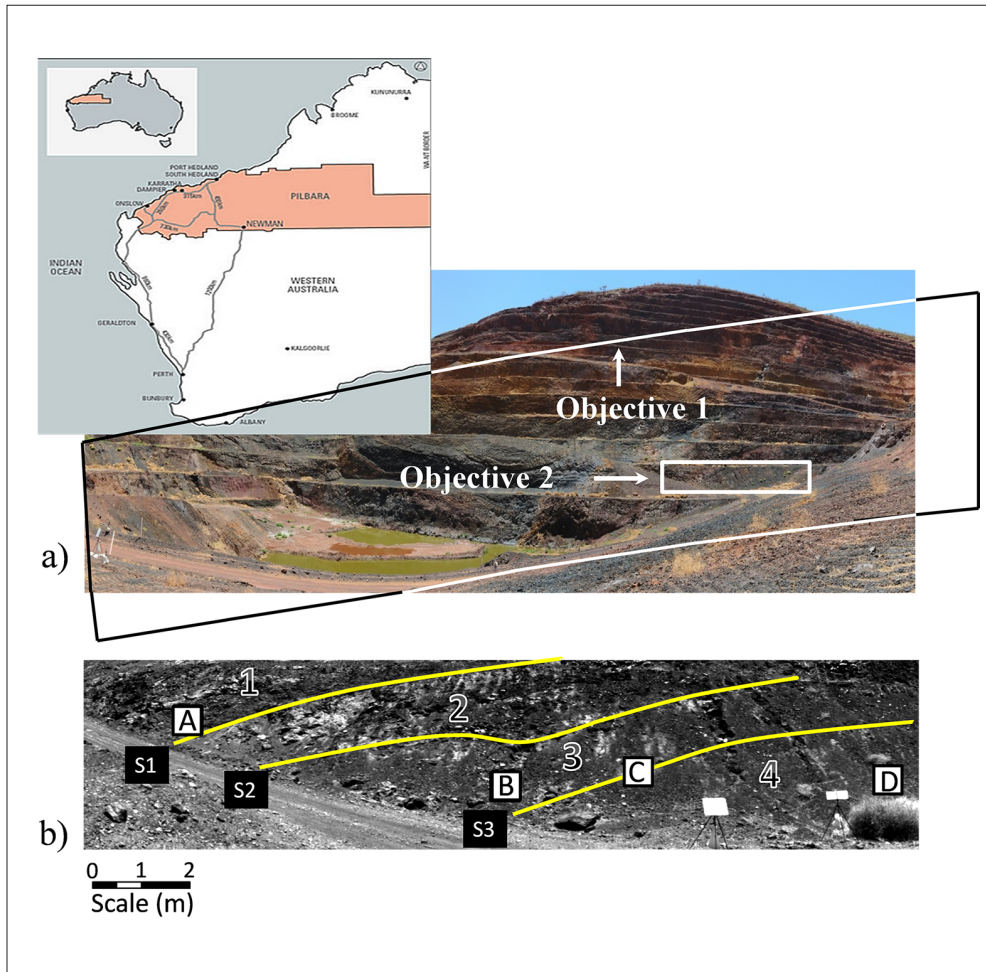


Figure 1 - Study area. (a) Location of the hyperspectral scan lines for Objectives 1 and 2 within the mine pit (inset: location of the Pilbara region within Australia); **(b)** A single hyperspectral image band (2000 nm) showing detailed mapping made in the field of the different geological units 1-4: banded iron formation (BIF; 1), mixed BIF and low grade hematite (2), low grade hematite (3) and high grade hematite (4). The mapped locations of the clay layers delineating the geological units are indicated (S1-S3). The location of the quadrats from where rock samples were acquired are indicated by the white rectangles (A-D).

The dark current signal was removed by subtraction from each spatial line of data at each band. Imagery was calibrated using the empirical line method [Smith and Milton, 1999]. The longest sensor-target distance was > 700 m, thus path radiance may have had a small impact on spectra. The empirical line method was therefore used to minimise the impact of path radiance in preference to the flat field approach which would remove only multiplicative effects. Calibration was done using the 80 % Teflon and 15 % Spectralon panels. Both panels had been spectrally characterised in the laboratory and their reflectance factors calculated. Pixels over the calibration panels were separately extracted and averaged

for each spectral band. The relationship (slope and intercept) between the panel reflectance and averaged pixel (i.e. DN values) was determined for each band. The slope and intercept was then used to convert DN to reflectance using a simple linear model:

$$\text{Reflectance band}_i = \text{DN band}_i * \text{aband}_i + \text{bband}_i \quad [1]$$

where:

DN is the digital number of the i^{th} spectral band;

a = slope of the regression equation;

b = intercept of the regression equation.

Automated feature extraction

The image was filtered using a polynomial smoothing filter with a width of 8-bands [Savitzky and Golay, 1964]. All absorption features were placed on the same reference plane by normalising the reflectance. Normalised reflectance was obtained by dividing the reflectance at each wavelength by the reflectance of the spectral continuum at that wavelength [Clark and Roush, 1984]. Automated feature extraction was then used to identify the strongest (i.e. deepest) absorption feature in the normalised spectra between 2041 and 2380 nm and parameterise it in terms of its wavelength position, depth and width. Wavelengths were constrained to this range to avoid increasing amounts of noise towards shorter or longer wavelengths caused by atmospheric water absorption and decreasing solar irradiance. Two thresholds were used. First, a feature is 'found' only if the hull-quotient value of the absorption feature minimum is less than 0.95. Preliminary work determined that this removed spurious absorptions caused by increasing noise towards longer wavelengths from consideration. Second, a brightness threshold was set to remove from consideration all spectra which had an average brightness of less than 0.08 (i.e. 8 % reflectance). Spectra with a brightness of less than this threshold had a very low signal-to-noise ratio resulting in AFE 'finding' spurious absorption features. Depth was calculated as 1 minus the normalised reflectance at the band centre. This is arithmetically equivalent to the method proposed by Clark and Roush [1984]. Width was calculated by determining the normalised reflectance at half of the depth of the feature. The corresponding wavelengths at this reflectance were calculated by interpolation and feature width determined by subtracting the long- from the short-wavelength. Wavelength position, depth and width for each pixel spectrum were described quantitatively in separate grey-scale images.

LiDAR data

For Objective 1, LiDAR scans of the mine pit were acquired to generate 3D point clouds of the scene. The laser scanner (Riegl LMS-Z620) was placed in close proximity to the hyperspectral sensor. The LiDAR scans comprised two scans made from the same position. The first scan covered 180 degrees and contained 4.5 million points. The second scan covered an additional 90 degrees and contained 2.5 million points. The scans covered a range from approximately 3 m to 700 m from the sensor. The average angular resolution of the sensor was 0.04 degrees.

Registration of AFE parameters with LiDAR data

For Objective 1, the AFE parameter images derived from the hyperspectral images were automatically registered to the point cloud from the LiDAR using the method of Taylor et al. [2013]. The method automatically determined the location and orientation of the camera relative to the LiDAR, as well as the intrinsic parameters of the camera using a single band from the hyperspectral data cube. In this case the 970 nm band was used as this was the closest to the frequency used by the LiDAR and allowed for the greatest correlation between the image intensities and the LiDAR's intensity of return. To align the sensor outputs, a camera model was created that projects the LiDAR data onto the hyperspectral image. The quality of the alignment between the LiDAR and the hyperspectral image was evaluated by using a gradient orientation measure that compared the relative alignment of gradients. The unknown parameters of the camera model - in this case the location, orientation, focal length, principle point and radial distortion - were found using particle swarm optimisation, which maximised the gradient measure. The method used to align the sensors differed slightly from that presented in Taylor et al. [2013], in two key areas. Firstly the gradient for the LiDAR points was found by projecting the LiDAR points onto a sphere. These points were then interpolated to form an image which had a Sobel operator run on it to find the gradients. Secondly, lens distortion was included as a parameter of the optimisation. In the y direction the lens distortion was modeled as $y_{\text{distorted}} = d_1 y^2 + d_2 y^4$, where y is the y position in normalised image coordinates and d_1 and d_2 are the distortion parameters to be estimated. As the hyperspectral camera was a line scanner that rotates to form an image, distortions in the lens have no effect on the x axis of the image. The search space for the optimiser was formed around a rough guess as to the alignment from the location of the camera tripod in the LiDAR scan and observing the sensor outputs. The search space was set to have a range of 10 degrees for roll, pitch and yaw and 1 metre in the x, y and z dimensions. The focal length had a range of 100 pixels, the principle point a range of 40 pixels and the distortion parameters, d_1 and d_2 a range of 1. The source code used to do this can be found in Taylor et al. [2013].

An estimate of how reliable this calibration process was also generated. This was done by bootstrapping the LiDAR data before registering it with the camera data. Using the bootstrapping process the registration was performed 20 times with the results used to estimate the variance of the estimated camera parameters.

The area of the mine pit covered by each of the minerals mapped by AFE was calculated in two separate ways. First a simple estimate of the area was made from the 2D mineral map (wavelength position) from imagery prior to its registration with the LiDAR data (image area). Second, area was calculated from imagery of wavelength position after it was registered with the LiDAR scan (face surface area). To calculate the area from the point cloud, the space each point covers was calculated by assuming it was a square whose sides are the length of the median distance to the four closest neighbours. Small changes in the cameras position could have a large impact on the location of classified minerals. To account for this, the estimated variance in the camera parameters previously calculated was used to calculate a variance in the classified area using a Monte-Carlo sampling approach.

Results

Objective 1 - quantifying areal coverage of clay minerals in the mine pit

The accuracy of the registration between the LiDAR and camera was evaluated. As no ground truth exists for this dataset this was done by hand matching 10 distinctive points in the image with their corresponding point in the LiDAR scan (Fig. 2). Two measures of the accuracy of the points were made. The first is a simple pixelwise error made by measuring the distance between the corresponding points when the LiDAR points are projected onto the image. The second is the estimated ‘real world’ error (in metres) to which this corresponds. This was formed by dividing this pixel error by the camera focal length and multiplying by the distance to the LiDAR point. For the registration used we found a mean pixel error of 2.92 pixels and a mean distance error of 0.48 m. As the mine pit of interest was approximately 120 to 700 m from the camera and around 700 m wide this level of error in the registration was deemed to be acceptable.

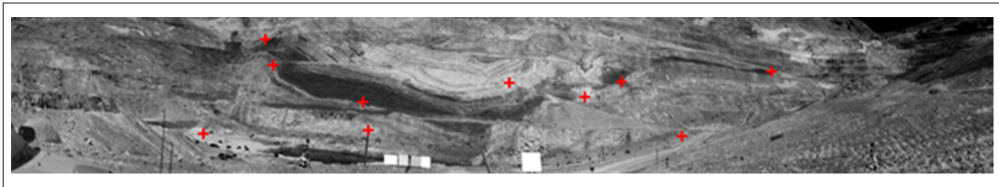


Figure 2 - Hand matched points (red crosses) used to evaluate the accuracy of the LiDAR camera registration.

Separate images quantifying the wavelength position of the deepest absorption feature and its depth were generated using AFE. On the basis of wavelength position, 7 minerals were identified (Fig. 3). The illite-smectites were identified by their main absorption at 2208 nm in combination with a weak absorption at 2235 nm. Ferruginous (Fe) smectite was identified by absorptions at 2288 nm and 2233 nm related to both Fe and Al in octahedral sites [Bishop et al., 2008]. Nontronite was identified by a single feature at 2282-2288 nm caused by Fe-OH and Kaolinite by the characteristic Al-OH absorption doublet at 2196 nm or 2202 nm [Crowley and Vergo, 1988]. Chlorite was identified by a broad absorption centred on 2319 nm. Talc had several sharp features between 2041 and 2380 nm but the strongest was at 2306 nm. Images of wavelength position, depth and width are shown in Figure 4. The wavelength parameter image shows distinct, narrow layers formed by several clay minerals including kaolinite but also much thicker (tens of metres) layers of nontronite were evident (Fig. 4a). Chlorite was present in discrete areas of the mine wall, mainly at the bottom of the synclinal fold. Large spatial variations in the abundance of clay minerals, indicated by the depth parameter image, were found across the mine wall (Fig. 4b). The strongest absorptions were found for the minerals Talc, Nontronite and Kaolinite and the weakest for Illite-smectite and Fe-smectite. The width of absorption features varied from about 35 nm for illite-smectite and nontronite to 135 nm for chlorite (Fig. 4c).

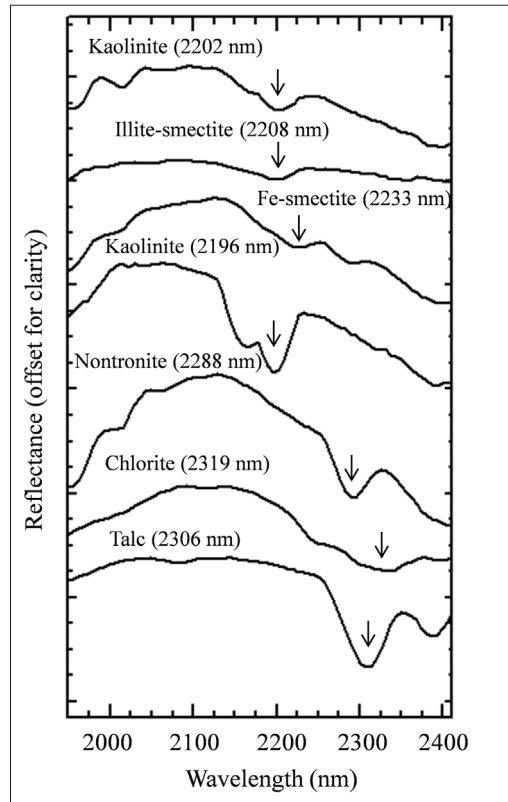


Figure 3 – Single image pixel spectra of minerals identified from the wavelength parameter image. Arrows indicate the centre of the deepest absorption in each spectrum.

Using the parameters from the projection of the hyperspectral image onto the LiDAR data, 2.5D maps of mineral distribution were created from the wavelength parameter image (Fig. 4a). From the 2D images (e.g., Fig. 4a) it is difficult to determine perspective in relation to the overall geometry of the mine pit. However, the 2.5D image clearly showed that the greatest spatial variation in the types of clay minerals occurred towards the base of the mine pit in a region of complex synclinal folding (Fig. 5). The LiDAR data allowed the real area of each classified mineral to be accurately estimated. The two estimates of area derived from the image data (image area and face surface area) were compared (Tab. 1, Fig. 6), and showed the estimates of area calculated from the 2D mineral maps were under- or over-estimated by as much as a factor of 2. Note that the changes in percent area classified as 2197 nm (kaolinite) and 2319 nm (chlorite) were particularly large. This is due to their distance from the hyperspectral imager. Kaolinite was mainly present in areas near the top of the mine pit, several hundred metres distant from the imager, causing them to appear far smaller in the image area estimates in comparison to the face surface estimates. The opposite effect occurs for chlorite which is closer to the sensor, towards the base of the synclinal fold.

Table 1 - Area classified as each mineral type, in terms of wavelength position. Standard deviation (SD) is shown for the Face Surface.

Wavelength Position	Image Area (Pixels)	Face Surface Area (m ²)	Image Area (%)	Face Surface Area (%)	Face Surface SD (%)
Unclassified	466110	73461	72.3	67.0	1.0
2197	54913	16351	8.5	14.9	0.8
2202	29753	5867	4.6	5.4	0.3
2220	6192	1251	1.0	1.1	0.3
2233	18134	3007	2.8	2.7	0.2
2288	39405	6318	6.1	5.8	0.4
2306	17331	2329	2.7	2.1	0.2
2319	12642	1053	2.0	1.0	0.1
Total	644480	109637	100	100	

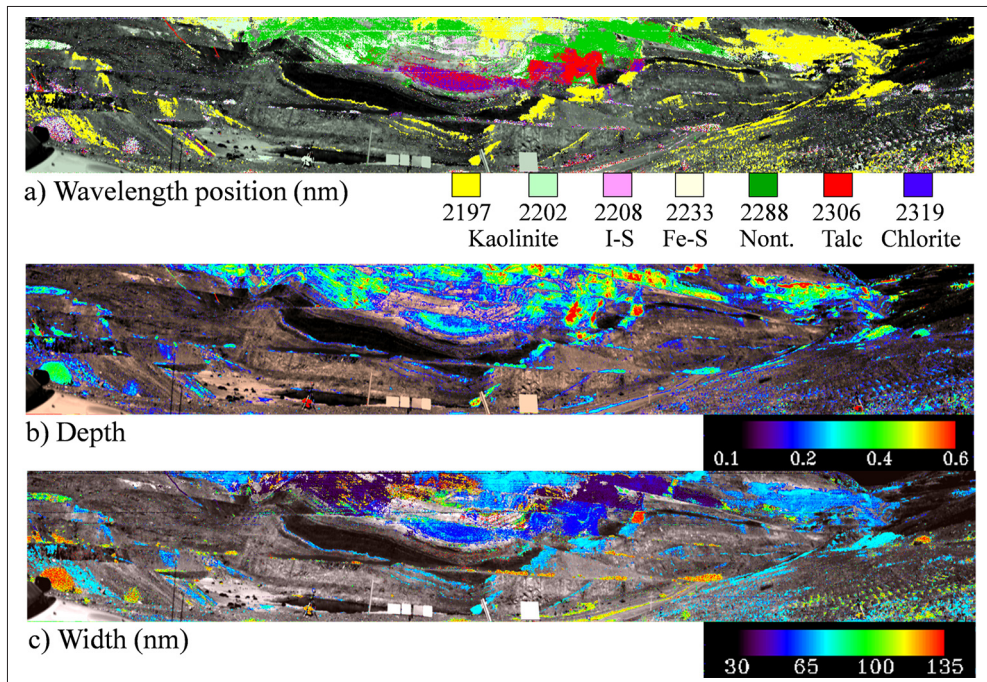


Figure 4 - AFE parameter images (Objective 1): (a) wavelength position; (b) depth; (c) width (nm). Identities of minerals associated with the different wavelength positions are shown in a): kaolinite; illite-smectite (I-S); ferruginous smectite (Fe-S); nontronite (Nont.); Talc; Chlorite.

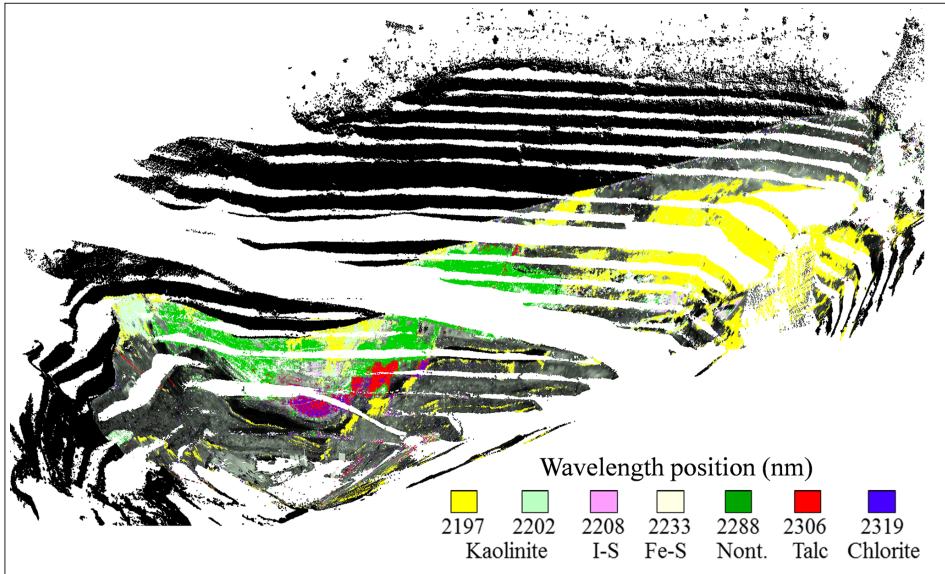


Figure 5 - Coloured point cloud of clay minerals for the large-scale mapping; wavelength position registered to the LiDAR data (Objective 1). Locations mapped by LiDAR but not the hyperspectral sensor are shown as black. Locations imaged by the hyperspectral sensor but where no absorption was found are shown in greyscale. Identities of minerals associated with the different wavelength positions are indicated in the colour key: kaolinite; illite-smectite (I-S); ferruginous smectite (Fe-S); nontronite (Nont.); Talc; Chlorite.

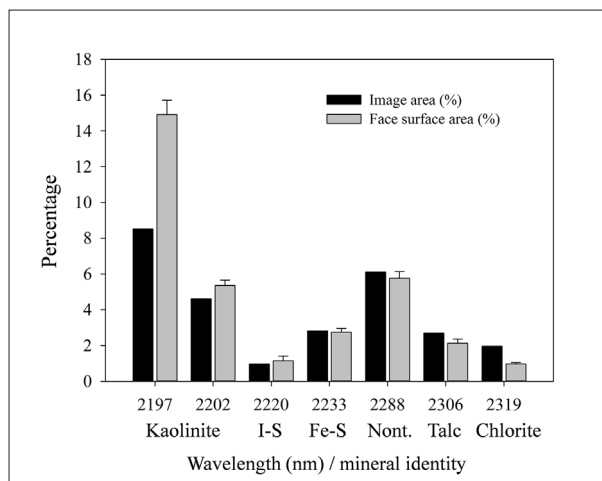


Figure 6 - Percent of the area classified as a given mineral for the 2D image plane (Image area) and fused with the LiDAR data (Face surface area). Mineral identities are shown below wavelengths on the horizontal axis: kaolinite; illite-smectite (I-S); ferruginous smectite (Fe-S); nontronite (Nont.). The error bars show the standard deviation or error in the projections of the hyperspectral image and LiDAR.

Objective 2 - Using clay layers to delineate geological units

Spectra from quadrats A (BIF), B (low grade hematite) and D (high grade hematite) have a similar curve shape and have large amounts of variability in reflectance, making these geological units difficult or impossible to distinguish based on their spectral characteristics alone (Fig. 7). The similarity in spectral curve shape occurs even though the relative amounts of minerals within the rocks are quite different (Tab. 2). Spatial variability in reflectance was largely attributable to spatial variability in incident radiation.

Table 2 - Percent weight of the dominant minerals within each quadrat (see Fig. 1b for context) derived from quantitative XRD. Note the presence of kaolinite in Quadrat C located over the shale band (S3).

Mineral	Quadrat A		Quadrat B		Quadrat C		Quadrat D	
	Average	SD	Average	SD	Average	SD	Average	SD
Goethite	14.30	15.26	2.62	1.79	14.22	13.80	-	-
Hematite	28.52	25.21	95.40	2.07	70.48	26.15	97.40	0.55
Kaolinite	-	-	-	-	11.40	17.28	-	-
Quartz	53.88	24.76	-	-	0.82	1.83	-	-

Four distinct geological units were identified on the mine face using a combination of the field mapping and the results from the X-ray diffraction analyses (Fig. 8a). These were un-mineralised Banded Iron Formation (BIF; Unit 1), low-grade hematite mixed with BIF (Unit 2), and higher-grade hematite (Units 3 and 4). AFE identified the 3 clay layers that were mapped in the field (S1, S2 and S3). AFE correctly identified Al-OH absorptions associated with these clay layers. The wavelength parameter image shows that the majority of absorption features were located at 2196 and 2202, associated with kaolinite and kaolinite-smectite (Fig. 8b). A few scattered pixels had absorption features at 2208 nm, suggestive of illite-smectite. The designation of kaolinite-smectite and kaolinite-illite was based entirely on their wavelength positions; these mixed-layer clays were not, however, identified in any of the XRD analyses. This may be due to the poor sensitivity of the XRD analyses from powdered samples. These assignments should therefore be treated with caution. In any event, all absorptions found by AFE in this image are associated with Al-OH and correspond to the correct location of the clay layers mapped in the field.

The wavelength positions of features in S1 (2202 nm) were, on average, different to those in S2 (2208 nm). Two narrower clay layers, not mapped in the field, were identified by AFE at the extreme left of the image. The clay absorptions mapped by AFE did not form contiguous linear features on the mine face. S1 and S2, in particular, had discontinuities in clay absorption along their length. This was, however, entirely consistent with field observations. The discontinuities in the clay layers indicate that the abundance of clays in these areas was small and that the absorptions were too weak to be included in the depth threshold used by AFE to identify coherent absorptions. The depth parameter image showed that clay layers S2 and S3 had deeper absorptions than did S1, indicating a greater abundance of the clays in these layers (Fig. 8c). Absorption feature width did not provide any useful information and is not therefore shown.

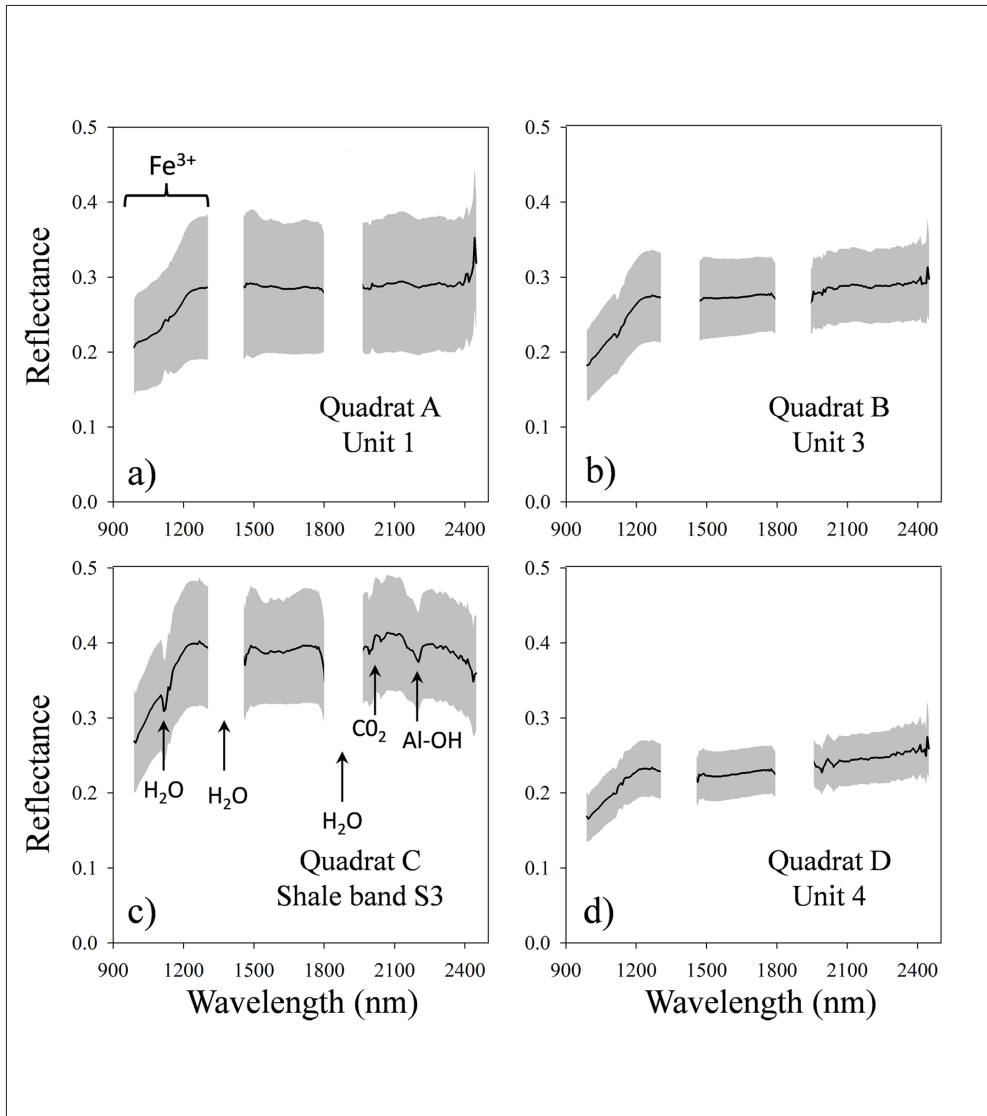


Figure 7 - Mean (\pm SD, grey area) spectra from pixels within each of the quadrats from which rock samples were acquired ($n = 700$; see Figure 1b and Table 2): (a) Quadrat A; (b) Quadrat B; (c) Quadrat C; (d) Quadrat D. The common feature to all spectra is the long-wave slope of the ferric iron (Fe^{3+}) crystal field absorption centred at ~ 900 nm (i.e. located to shorter wavelengths than those detected by the imaging sensor used in this study) is indicated in (a). The $Al-OH$ absorption feature associated with some clay minerals (kaolinite in this case) is shown in (c), together with the location of extraneous absorption features caused by atmospheric water and carbon dioxide. Note the spectral similarity and the large within-quadrat variability of spectral reflectance (SD) from different geological units (graphs a, b and d).

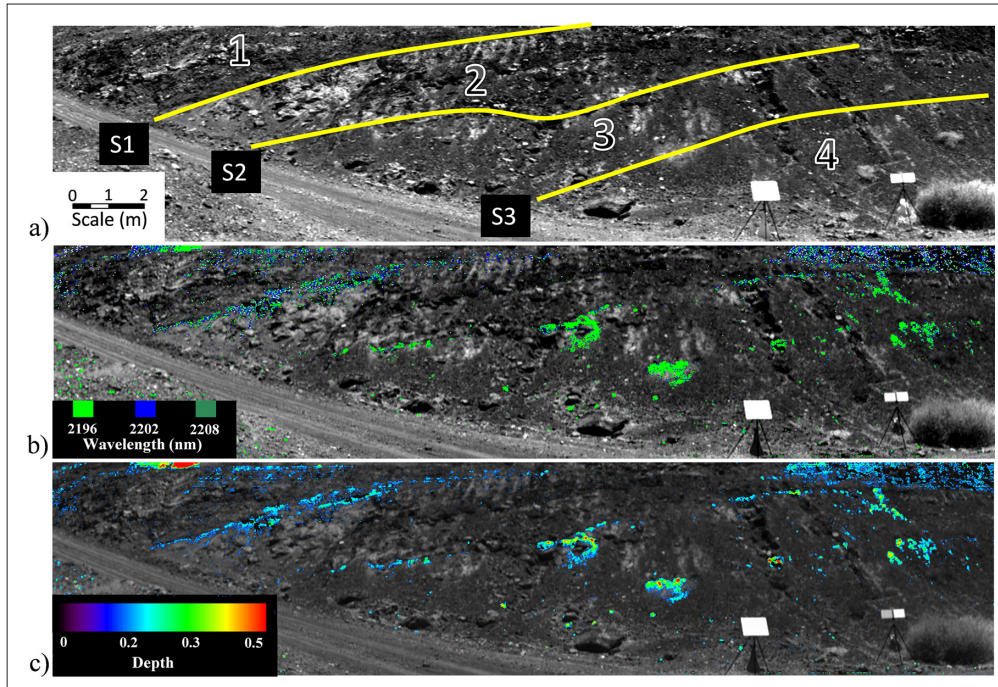


Figure 8 - Clay layers identified on a mine face by AFE (Objective 2): (a) Greyscale image with superimposed clay layers mapped from field observations (S1, S2 and S3) delineating units 1, 2, 3 and 4; (b) Wavelength parameter image; (c) depth parameter image. Scale is shown in a.

Discussion and conclusions

The advantage of AFE over other spectral analyses methods (e.g. the spectral angle mapper) is that it can be applied to any data acquired at SWIR wavelengths (2000 - 2500 nm) without the use of a spectral library or *a priori* knowledge of the particular scene in question. By quantifying the depth of absorption features it also enables estimates of the relative abundance of absorbing minerals to be made. It must, however, be recognised that AFE can have the disadvantage of ‘underusing’ the data by classifying minerals on the basis of wavelength position rather than the shape of the entire spectral curve. In this study we used three AFE parameters to describe the deepest absorption feature in each spectrum: wavelength position, depth and width. If the amount of spectral noise in the data is small then features of secondary or tertiary strength could be parameterised. Other parameters may also be quantified using AFE e.g. asymmetry and slope between the shoulders of the absorption.

Our choice of a mine pit with complex surface geometry provided a difficult test of the methods used to map minerals and to quantify their areal coverage for two reasons. First, the highly variable topography of the surface caused large variations in the amount of incident light which can affect spectral signatures in complex ways, potentially limiting our ability to extract relevant information from them. Second, the mine pit was large resulting in a continuum of different distances from the hyperspectral sensor to the target. Despite these difficulties, AFE in combination with co-registered LiDAR data enabled 2.5D maps

of mineralogy to be constructed for large sections on the mine pit providing detailed information on the identity and abundance of clay minerals. The automatic method used to register the hyperspectral and LiDAR data enabled accurate estimates of the area covered by each mineral to be determined. This factor, combined with the high spatial resolution of hyperspectral and LiDAR data and their contiguous nature provide a powerful approach to the quantitative mapping of large areas using data acquired from field-based platforms. The results from Objective 1 clearly show that meaningful quantitative information can be extracted from these data and highlight the errors which can result from simply estimating area of minerals from 2D maps.

In Objective 2 we used hyperspectral data to map clay layers on a mine face as a way of distinguishing geological zones which are of similar visual or spectral appearance. The three major clay layers identified from field mapping were all identified using AFE. This opens up the possibility for contextual classification of geological units based on the location of these clay layers in the stratigraphy. The ability to combine, automatically, products derived from hyperspectral imagery with LiDAR data greatly improves the scope of applications for its use, as observed by Kurz et al. [2011]. For example, combining information on clay minerals with information on aspects of geometry (e.g. slope, aspect) enables pertinent, spatially referenced information to be incorporated into models of slope stability. Work is currently underway to determine the best ways in which information from the various absorption feature parameters can be combined into meaningful thematic maps.

The development of hyperspectral imaging systems for use in the field has opened up new possibilities for its use in quantitative mapping of minerals on natural and artificial vertical geological surfaces.

Acknowledgement

This work has been funded by the Australian Centre for Field Robotics and the Rio Tinto Centre for mine Automation. We thank Dr Geoff Carter for his help in the field.

References

- Bishop J.L., Lane M.D., Dyar M.D., Brown A.J. (2008) - *Reflectance and emission spectroscopy study of four groups of phyllosilicates: smectites, kaolinite-serpentines, chlorites and micas*. Clay minerals, 43: 35-54. doi: <http://dx.doi.org/10.1180/claymin.2008.043.1.03>.
- Buckley S.J., Kurz T.H., Howell J.A., Schneider D. (2013) - *Terrestrial lidar and hyperspectral data fusion products for geological outcrop analysis*. Computers and Geosciences, 54: 249-258. doi: <http://dx.doi.org/10.1016/j.cageo.2013.01.018>.
- Clark R.N., Roush T.L. (1984) - *Reflectance spectroscopy: Quantitative analysis techniques for remote sensing applications*. Journal of Geophysical Research, 89 (B7): 6329-6340. doi: <http://dx.doi.org/10.1029/JB089iB07p06329>.
- Cornforth D.H. (2005) - *Landslides in Practice - Investigation, Analysis, and Remedial/Preventative Options in Soils*, Hoboken, NJ, USA, John Wiley and Sons.
- Crósta A.P., Sabine C., Taranik J.V. (1998) - *Hydrothermal Alteration Mapping at Bodie, California, Using AVIRIS Hyperspectral Data*. Remote Sensing of Environment, 65 (3): 309-319. doi: [http://dx.doi.org/10.1016/s0034-4257\(98\)00040-6](http://dx.doi.org/10.1016/s0034-4257(98)00040-6).
- Crowley J.K., Vergo N. (1988) - *Near-infrared reflectance spectra of mixtures of kaolin-*

- group minerals: Use in clay mineral studies*. Clays and Clay minerals, 36 (4): 310-316. doi: <http://dx.doi.org/10.1346/CCMN.1988.0360404>.
- Gill J.D., West M.W., Noe D.C., Olsen H.W., McCarty D.K. (1996) - *Geologic control of severe expansive clay damage to a subdivision in the Pierre Shale, Southwest Denver Metropolitan area, Colorado*. Clays and Clay Minerals, 44 (4): 530-539. doi: <http://dx.doi.org/10.1346/CCMN.1996.0440412>.
- Goetz A.F.H., Chabrilat S., Lu Z. (2001) - *Field reflectance spectrometry for detection of swelling clays at construction sites*. Field Analytical Chemistry and Technology, 5 (3): 143-155. doi: <http://dx.doi.org/10.1002/fact.1015>.
- Hancox G.T. (2008) - *The 1979 Abbotsford Landslide, Dunedin, New Zealand: a retrospective look at its nature and causes*. Landslides, 5: 177-188. doi: <http://dx.doi.org/10.1007/s10346-007-0097-9>.
- Hartley R.I., Zisserman A. (2004) - *Multiple View Geometry in Computer Vision*. Cambridge, UK, Cambridge University Press. doi: <http://dx.doi.org/10.1017/CBO9780511811685>.
- Hutchinson J.N. (1961) - *A Landslide on a Thin Layer of Quick Clay at Furre, Central Norway*. Geotechnique, 11 (2): 69-94. doi: <http://dx.doi.org/10.1680/geot.1961.11.2.69>.
- Kruse F.A. (1988) - *Use of airborne imaging spectrometer data to map minerals associated with hydrothermally altered rocks in the northern grapevine mountains, Nevada, and California*. Remote Sensing of Environment, 24 (1): 31-51. doi: [http://dx.doi.org/10.1016/0034-4257\(88\)90004-1](http://dx.doi.org/10.1016/0034-4257(88)90004-1).
- Kurz T.H., Buckley S.J., Howell J.A. (2013) - *Close-range hyperspectral imaging for geological field studies: Workflow and methods*. International Journal of Remote Sensing, 34 (5): 1798-1822. doi: <http://dx.doi.org/10.1080/01431161.2012.727039>.
- Kurz T.H., Buckley S.J., Howell J.A., Schneider D. (2011) - *Integration of panoramic hyperspectral imaging with terrestrial lidar data*. The Photogrammetric Record, 26 (134): 212-228. doi: <http://dx.doi.org/10.1111/j.1477-9730.2011.00632.x>.
- Lagacherie P., Baret F., Feret J.-B., Madeira Netto J., Robbez-Masson J.M. (2008) - *Estimation of soil clay and calcium carbonate using laboratory, field and airborne hyperspectral measurements*. Remote Sensing of Environment, 112 (3): 825-835. doi: <http://dx.doi.org/10.1016/j.rse.2007.06.014>.
- Martinez-Alonso S., Rustad J.R., Goetz A.F.H. (2002) - *Ab initio quantum mechanical modeling of infrared vibrational frequencies of the OH group in dioctahedral phyllosilicates. Part II: Main physical factors governing the OH vibrations*. American Mineralogist, 87 (8-9): 1224-1234.
- Murphy R., Schneider S., Monteiro S. (2014) - *Mapping Layers of Clay in a Vertical Geological Surface Using Hyperspectral Imagery: Variability in Parameters of SWIR Absorption Features under Different Conditions of Illumination*. Remote Sensing, 6 (9): 9104-9129. doi: <http://dx.doi.org/10.3390/rs6099104>.
- Murphy R.J. (1995) - *The effects of surficial vegetation cover on mineral absorption feature parameters*. International Journal of Remote Sensing, 16 (12): 2153-2164. doi: <http://dx.doi.org/10.1080/01431169508954548>.
- Murphy R.J., Monteiro S.T. (2013) - *Mapping the distribution of ferric iron minerals on a vertical mine face using derivative analysis of hyperspectral imagery (430-970 nm)*. ISPRS Journal of Photogrammetry and Remote Sensing, 75: 29-39. doi: <http://dx.doi.org/10.1016/j.isprsjprs.2013.05.001>.

- org/10.1016/j.isprsjprs.2012.09.014.
- Murphy R.J., Monteiro S.T., Schneider S. (2012) - *Evaluating Classification Techniques for Mapping Vertical Geology Using Field-Based Hyperspectral Sensors*. IEEE Transactions on Geoscience and Remote Sensing, 50 (8): 3066-3080. doi: <http://dx.doi.org/10.1109/tgrs.2011.2178419>.
- Savitzky A., Golay M.J.E. (1964) - *Smoothing and differentiation of data by simplified least squares procedures*. Analytical Chemistry, 36 (8): 1627-1639. doi: <http://dx.doi.org/10.1021/ac60214a047>.
- Smith G.M., Milton E.J. (1999) - *The use of the empirical line method to calibrate remotely sensed data to reflectance*. International Journal of Remote Sensing, 20 (13): 2653-2662. doi: <http://dx.doi.org/10.1080/014311699211994>.
- Taylor Z., Nieto J., Johnson D. (2013) - *Automatic calibration of multi-modal sensor systems using a gradient orientation measure*. IEEE/RSJ International Conference on Intelligent Robots and Systems, Tokyo, Japan. <http://dx.doi.org/10.1109/IROS.2013.6696516>.
- Zhang Q., Pless R. (2004) - *Extrinsic calibration of a camera and laser range finder (improves camera calibration)*. IEEE/RSJ International Conference on Intelligent Robots and Systems (IROS 2004), Sendai, Japan.